Energy Balance of a Semicrystalline Polymer During Local Plastic Deformation

Jean Michel Muracciole, Bertrand Wattrisse, André Chrysochoos

Energy Balance of a Semicrystalline Polymer During Local Plastic Deformation

J.-M. Muracciole*†, B. Wattrisse* and A. Chrysochoos*†

*Mechanics and Civil Engineering Laboratory, Montpellier II University, CC 048, Place E. Bataillon, 34095 Montpellier, Cedex 05, France

†Polytech'Montpellier, Material Department, Montpellier II University, CC 419, Place E. Bataillon, 34095 Montpellier, Cedex 05, France

ABSTRACT: This paper, in a first part, presents the characteristics of a new experimental set-up using digital image correlation (DIC) and infrared thermography (IRT). In a second part, the kinematical data, obtained by DIC, are used to track the material surface element temperature variations deduced from thermal images. They are then combined to construct the local energy balance. To illustrate the interest of such an approach, the paper then describes the calorimetric effects accompanying the propagation of necking in a plasticised PolyAmide 11. A thermodynamic analysis of cyclic loading finally aims to show the existence of an entropic elastic effect generally associated with rubber-like materials.

KEY WORDS: *digital image correlation, infrared thermography, necking, polymers, rubber elasticity*

Introduction

The cold drawing of semi-crystalline polymers was first observed in the early 1930s by Carothers and Hill [1]. Ever since, various attempts have been made to explain this phenomenon in terms of crystallinity modification. This behaviour, usually related to a rearrangement of the crystallites, depends on the nature of the stretched materials. In some polymers, during necking, parts of the chains in crystalline blocks are unfolded and transfer into an amorphous phase with more or less orientation (see Refs [2, 3]). In others [4], the polymers exhibit crystallite realignment. Waddon and Karttunen [5] emphasise solid–solid phase transition. Nevertheless, there is a general agreement that a local rise in temperature occurs in the neck shoulders.

To perform an energy balance during such local phenomena, an experimental approach has been developed for the material behaviour characterisation which combines digital image correlation (DIC) with infrared thermography (IRT). The DIC techniques give access to displacement measurement and deformation fields, while the thermal images enable, under certain conditions, an estimation of the distribution of heat sources induced by the deformation process. Those thermal images were recorded using an infrared camera and a specific pixel calibration method described in Ref. [6]. A specialised electronic system was performed to get a simultaneous recording of speckle and infrared images. A combined treatment of kinematics and thermal data then allowed the temperature of material surface elements (MSEs – the 2D equivalent of the material volume elements when working on thin flat specimen) to be tracked and local energy balances to be constructed. This processing is well adapted for studying the thermomechanical behaviour of a material when localisation mechanisms occur at the observation scale fixed by the optical lenses. Applications to steels and polymers have already been carried out for monotonic quasi-static loadings [7, 8].

In what follows, after having recalled the main characteristics of the experimental arrangement, the protocol defined to compute the heat sources is presented taking into account the existence of localisation zones. To illustrate this, tension tests on plasticised Polyamide 11 (PA11) samples are considered. For this kind of material, the necking zone spreads out during tension stages. Using thermal and kinematical data, the thermomechanical coupling effects that appear in the necking zone during a cyclic loading around a given tension state are analysed.

Energy balance

Generalised standard materials formalism is used to derive the local heat equation [9]. Within such a framework, the equilibrium state of each material volume element is characterised by a set of n state variables. The chosen state variables are: T the absolute temperature, ε a strain tensor and $(\alpha_1,\ldots,\alpha_{n-2})$ the $n-2$ scalar components of the vector α of 'internal'

variables that sum up the microstructural state of the material. By construction, the thermodynamic potential is the Helmholtz free-energy ψ. Combining both the first and second principles of thermodynamics, the local heat equation reads:

$$\rho C\left(\frac{\partial T}{\partial t}+v\ \mathrm{grad}\ T\right)-\mathrm{div}(k\ \mathrm{grad}\ T)=\underbrace{\rho T\frac{\partial^2\psi}{\partial T\partial\varepsilon}:\dot{\varepsilon}+\rho T\frac{\partial^2\psi}{\partial T\partial\alpha}:\dot{\alpha}}_{w^{\bullet}_{\mathrm{the}}+w^{\bullet}_{\mathrm{thc}}}+\underbrace{\left(\sigma-\rho\frac{\partial\psi}{\partial\varepsilon}\right):\dot{\varepsilon}-\rho\frac{\partial\psi}{\partial\alpha}:\dot{\alpha}}_{d_1}+r_{\mathrm{e}} \tag{1}$$

where ρ is the mass density, C the specific heat, v the velocity vector, k the material conduction tensor and the operator (:) denotes the double contracted product of two tensors.

The thermomechanical coupling sources and the intrinsic dissipation d_1 have been grouped in the right-hand side of Equation (1). The symbol $(\,)^{\bullet}$ means that the variation of $(\,)$ is path dependent. For the polyamide considered here, one of the coupling sources is $w^{\bullet}_{\mathrm{the}}$, the source associated with the thermoelastic effect due to the thermo-dilatability of the material, as first identified by Lord Kelvin [10]. It should be noted that other coupling sources $w^{\bullet}_{\mathrm{thc}}$ may exist and represent possible interactions between temperature and microstructure. For instance, in the case of PA11, true evidence of another coupling source is shown in this paper. This coupling will be in phase with the mechanical cyclic loading, in contrast to the classical thermoelastic effect which is out of phase with the loading [10–14].

Per unit volume, the intrinsic dissipation d_1 is the difference between the rate of deformation energy $w^{\bullet}_{\mathrm{def}}=\sigma:D$ (where σ is the Cauchy stress tensor and D the strain rate tensor) and the sum of elastic and stored energy rates $w^{\bullet}_{\mathrm{e}}+w^{\bullet}_{\mathrm{s}}=\rho\psi_{,\varepsilon}\dot{\varepsilon}+\rho\psi_{,\alpha}\dot{\alpha}$. At finite strain, the chosen strain variable ε is the Hencky strain tensor.

Finally, considering Fourier's law of heat conduction ($q=-k\ \mathrm{grad}\ T$), the left-hand side of Equation (1) becomes a partial derivative operator applied to temperature. Its estimate then leads to a local determination of the overall heat source $w^{\bullet}_{\mathrm{h}}=w^{\bullet}_{\mathrm{the}}+w^{\bullet}_{\mathrm{thc}}+d_1$.

Experimental design and image processing

The experimental set-up involved a servo hydraulic testing machine (MTS 810 frame 100 kN, load cell ±25 kN), an IRFPA camera (Cedip Infrared Systems, Jade 3, working in the 3–5 μm range) and a visible CCD camera (Camelia, 8M, Atmel). The lens axes of the cameras were kept fixed and perpendicular to both sides of the sample surface. A special electronic master–slave system was developed to ensure a perfect synchronisation of the frame grabbing of the two cameras. With this system, any one of the two cameras can be either slave or master. In these particular experiments, the CCD camera is the master camera. Moreover, the SYNCHROCAM system enabled simultaneous recording of various analogical signals (force, cross-head displacement, etc.) provided by the testing machine. It also sets the data-capture frequency: the frame rate of the master camera can be set, according to the camera specification, from one frame per hour up to 500 frames per second. Here, the master camera captured visible images at 1 Hz, while the IRFPA slave camera worked at 10 Hz. Finally, the acquisition time accuracy is better than 10^{-4} s which is sufficient for classical mechanical tests. The main characteristics of the two cameras are given in Table 1.

Kinematical fields

Speckle image processing gives the time evolution of various kinematical variables. White light and artificial speckle using painted spots were utilised in this work. The size of the speckle spot is estimated as the radius at half height of the autocorrelation function. It is about three pixels here: the CCD scale factor is 37.1 μm pix^{-1}, while the IR scale factor is 698.4 μm pix^{-1}. The camera must be carefully set so that the CCD detector remains parallel to the sample surface. Indeed, each out-of-plane movement (translation or rotation) produces a parallax error which distorts the images. The distance between the camera and the specimen is around 300 mm and a typical error on the strain measurements due to the setting up of the camera was about 1 10^{-4}–2 10^{-4}.

The scale calibration process uses the same calibrated target for IR and CCD cameras. Several specific points of this target are localised in the IR and CCD images. This establishes a correspondence between IR and CCD images. Then, each IR point position at any time can be located in the CCD coordinates.

Table 1: Main characteristics of cameras

	Image size (pixels)	Pixel size (μm^2)	Maximum frame rate (Hz)
Camelia 8M	3500 × 2300	10 × 10	2.7
Cedip Jade 3	240 × 320	30 × 30	250

The image processing was systematically performed in two steps after the test.

- *First step*. The displacement field was estimated. Generally, the displacement of each point located on the surface of the sample has three components: two in-plane components, say U and V and one out-of-plane component, say W. In Figure 1, (L_0, l_0, e_0) define the initial geometry of the sample test section, while (X, Y, Z) and (x, y, z) denote, respectively, the Lagrangian coordinates and Eulerian coordinates. The components U and V were directly computed by a DIC [15].
- *Second step*. The strains (or the strain rates) were then derived from the displacements by space (and time) differentiation. Each computational step used particular numerical processing. The reader interested in this subject is referred to Ref. [15].

To achieve accurate strain measurements, the displacement field must be filtered before any differentiation. A fitting technique based on a local least-squares (linear or quadratic) approximation of the discrete displacement data was chosen which also allows the computation of the derivatives. The choice of the approximation zone (AZ) is very important in the differentiation process. The optimised AZ depends on the signal-to-noise ratio and the amplitude of the sought derivatives: the final optimised AZ size was 1.484 mm in height and 0.297 mm in width due to the specimen length and width ratio.

Using standard parameters, the accuracy on the displacement calculation was about 5 10^{-2} pixel and the accuracy on the strain measurement was 5 10^{-4}.

Temperature and heat source fields

In the framework of the experiments, several hypotheses were made. First, it was confirmed that the external heat supply remained time independent so that: $r_e = -k\,\Delta T_0$ where T_0 is the equilibrium temperature field of the sample. Besides, for tests performed on thin flat specimens, Saurel [16] showed that the temperature measured at the sample surface remains very close to the depth-wise averaged temperature.

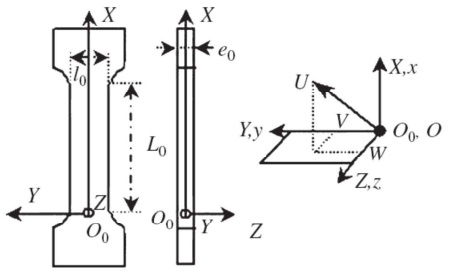

Figure 1: Frames, coordinates and specimen geometry $e_0 = 4$ mm, $l_0 = 10$ mm and $L_0 = 50$ mm

Taking into account all these hypotheses and integrating Equation (1) throughout the thickness of the specimen, the heat equation can be markedly simplified into a two-dimensional partial derivative equation

$$\rho C\left(\frac{\partial \theta}{\partial t} + v\ \text{grad}\ \theta + \frac{\theta}{\tau_{th}}\right) - k\ \Delta\theta = w_h^{\bullet} \qquad (2)$$

where $\theta = \overline{T - T_0}$ is the difference between T and T_0, averaged according to thickness, and τ_{th} is a time constant characterising heat losses perpendicular to the plane of the specimen. The heat conduction in the plane is taken into account by the two-dimensional Laplacian operator Δ.

With the thermal data, monitored on the as-received moulded surface of the specimens, being discrete and noisy, the differential operator was traditionally estimated by low-pass filtering and derived according to the properties of discrete Fourier transform and Fourier series [17]. To facilitate the coupling of numerical methods developed for kinematical and thermal data processing, a local least-squares fitting technique was chosen to calculate the left-hand side of Equation (2). The thermal data were spatially approximated by a parabolic function, corresponding to locally constant conduction heat losses in the neighbourhood of each pixel of the thermal image. As already mentioned, the dimensions of AZ affect the data fitting efficiency, and thus may influence the operator estimate. In the initial configuration, the AZ used for the thermal data was 3.71×0.742 mm.

In this work, the relative position of the sensors of the cameras is obtained, before the test, by the scale calibration process to determine the correspondence between IR and CCD images. The displacement data were, then, also used for the processing of thermal images to track the same material zone as the one observed by the CCD camera. With the mapping between the deformed region and the un-deformed configuration being established, the temperature maps are redrawn in the un-deformed configuration. This allowed the convective terms of the material time derivative of the temperature to be accounted for throughout the test.

Tests and results

Tensile tests were performed at room temperature on ISO R527 PA11 samples (see Figure 1). PA11 is a thermoplastic semi-crystalline polymer with a

triclinic phase and, at room temperature, a glassy amorphous phase. This raw material has undergone an ageing processing. The glass transition associated with the transition of the amorphous phase occurs at around 45 °C according to the material provider. Other material constants are $\rho = 1100$ kg m^{-3}, $C = 1480$ J kg^{-1} K^{-1} and $k = 0.2$ W m^{-1} K^{-1}.

Figure 2 shows the macroscopic mechanical response of the material during the test (load–displacement curve). The tests consisted of a velocity-controlled loading (imposed strain rate of around 8 10^{-3} s^{-1}; cf. Figure 3A) until the displacement reached 82.5 mm. Then, the control mode was switched to load, and nine sinusoidal cycles were completed (force amplitude 600 N and time period 5 s). The sample fracture occurred at the beginning of the 10th cycle during the loading phase.

The plateau in Figure 2 indicates that this material develops a localised neck in tension. The load cycles were performed after the development of the neck to characterise the thermomechanical behaviour of the material at large strains, when the macromolecular chains are highly stretched [18–20]. As the oriented chain is much stiffer than the unoriented one, the orientation mechanism leads to a neck propagation phenomenon. The increase in material stiffness limits the narrowing of the necked zone. To further extend the specimen elongation, the neck must move, drawing material from the unnecked region: the strain rate is then localised in the neck shoulders, while it remains approximately equal to zero within and outside these necking zones, cf. Figure 3B. Due to the poor thermal conductivity of the material, the position and size of localisation can be seen where there are important temperature gradients on the deformed or un-deformed configurations in Figure 4.

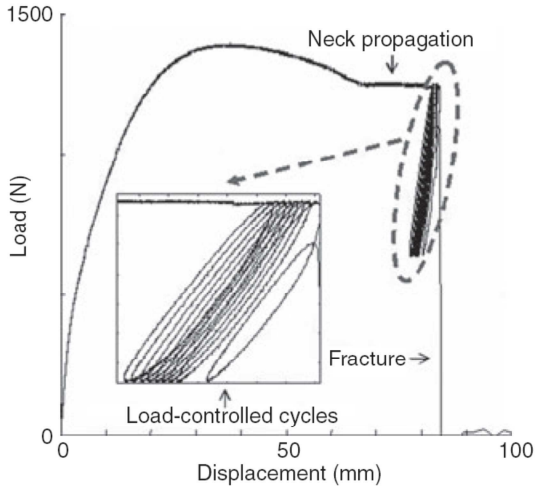

Figure 2: Mechanical response of PA11 sample ($T_0 = 25$ °C)

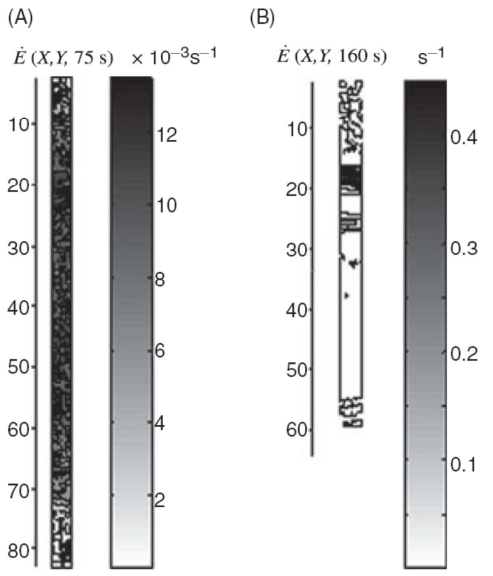

Figure 3: Strain-rate distribution in the un-deformed configuration at (A) $t = 75$ s, (B) $t = 165$ s

The necking is consequently associated with a heterogeneous response of the material. The concentration of heat sources in the neck shoulders and the low diffusivity of the polymer studied generate those temperature gradients that must be taken into account in the computation of the heat sources [8]. With the measurement fields being relatively homogeneous according to the specimen width, the time course of the data profiles captured along the longitudinal axis of the specimen was plotted.

The space–time charts (Figures 4–6) are constructed with the abscissa representing the time and the ordinate the longitudinal sample axis. The engineering stress $\sigma_0(t) = F(t)/(l_0 e_0)$, where $F(t)$ stands for the applied load as a function of time, was superimposed to illustrate the specimen global mechanical response to link the local patterns of the measurements to the loading state of the sample.

Figure 4A presents the time evolution of a crude thermo-profile directly extracted from infrared data files (Eulerian configuration). The room temperature is around 300 K. As the camera is fixed, each pixel no longer corresponds to a fixed MSE as soon as the strain becomes important. The paths of four MSEs named A, B, C and D are plotted to illustrate this. Note that the maximum amplitude of the temperature variations reaches more than 20 °C at point A, which fully justifies the choice of an anisothermal thermomechanical framework. Furthermore, this temperature increase is sufficient to warm the material up to the glass transition temperature in the neighbourhood of the neck.

With the displacement field being known, it is possible to track the temperature of any material

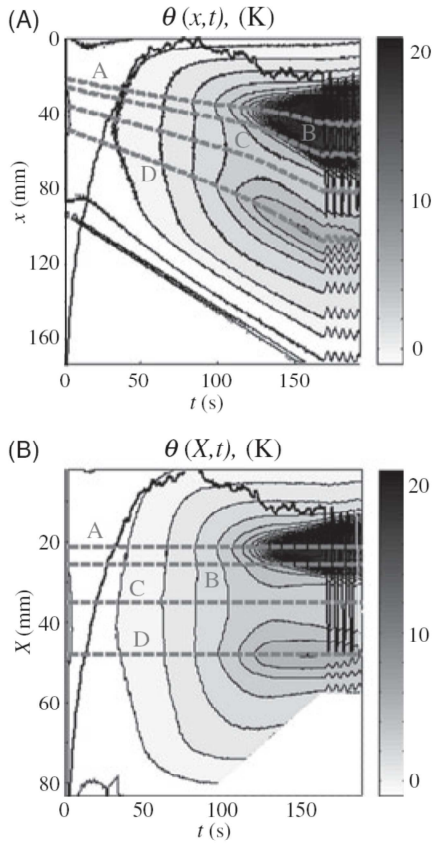

Figure 4: Time course of: (A) $\theta(x,t)$, (B) $\theta(X,t)$

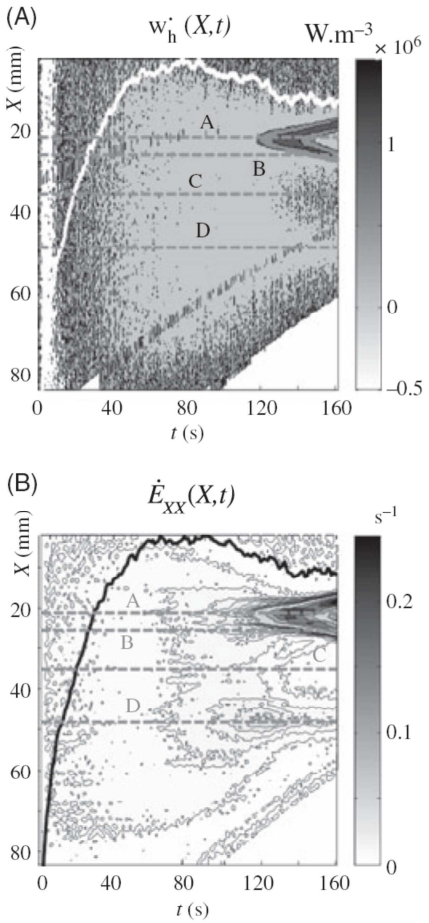

Figure 5: Time course of: (A) $w_h^{\bullet}(X,t)$, (B) $\dot{E}_{XX}(X,t)$

zone. Figure 4B shows the thermal data presented in Figure 4A, once the displacements have been taken into account. The paths of MSEs, A, B, C and D, henceforth correspond to horizontal straight lines (Lagrangian configuration).

The progressive narrowing of temperature level curves is difficult to interpret because of heat diffusion. The temperature is not completely intrinsic to the material behaviour, contrary to the heat sources. Figure 5A shows the time evolution of the corresponding heat sources profile during the test. At the beginning of the test, the profiles of the distribution of $w_h^{\bullet}$ is rather homogeneous and negative in accordance with classical thermoelastic behaviour during a simple tensile test. Then, profiles of $w_h^{\bullet}$ become positive and concentrate, to give way to the localised necking. This change of sign is related to the development of positive heat sources associated with dissipative mechanisms (i.e. viscosity and plasticity). The beginning of the plateau corresponds to the inception of two necking lips: the upper one moves upward to the upper grip (located at the top of Figure 5A) and the lower one moves downward to the lower grip (located at the bottom of the Figure 5A). Figure 5B illustrates the space–time evolution of the longitudinal strain-rate component, $\dot{E}_{XX}(X,t)$, of the Green–Lagrange tensor. The heat sources and strain-rate distributions are very similar: the higher the strain rate, the larger the heat source intensity, and thus, the larger the temperature variations.

The paths of the four spotted MSEs, A, B, C and D, are plotted in Figure 5. A is associated with the inception of the necking. At the end of the monotonic loading, A is thus located in the middle of the necked zone. B corresponds to the location reached by the lower neck shoulder at the end of the monotonic loading. As shown in Figure 5B, D has been chosen in the middle of a second localisation zone. Finally, C is set between B and D, in a region not yet influenced by the necking.

Figure 5A and B represents the distribution of the heat sources during the first five cycles. It is observed that the heat sources in the selected MSEs are negative when the applied load decreases and positive when it increases.

The oscillating part of the responses of the four points during the cyclic loading can be associated with coupling mechanisms. The measured heat sources are negative when the specimen is unloaded and positive otherwise: contrary to the classical thermoelastic sources, this coupling term is in phase with the mechanical loading as observed in the case

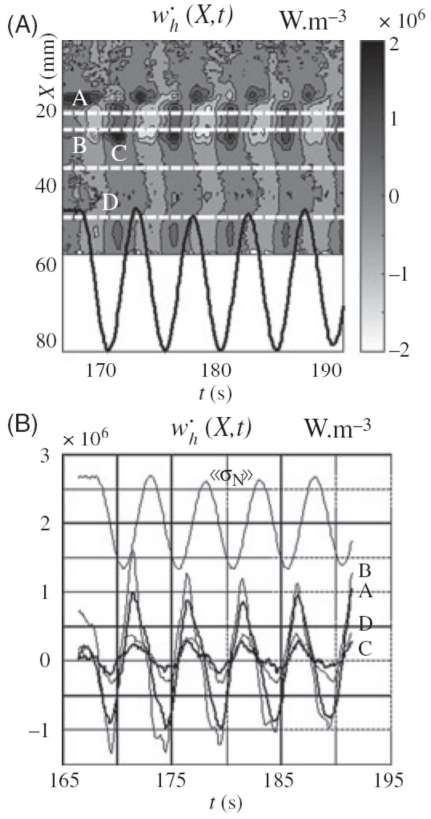

Figure 6: (A) Time course of $w_h^{\bullet}(X,t)$ during the first cycles. (B) Time evolution of sources for the different MSEs

of rubber-like materials [11–14]. The amplitude difference can be interpreted as the point-to-point difference in the competition between two opposite coupling effects: classical thermoelasticity (out of phase with the loading) and rubber elasticity (in phase).

Concluding comments

Some polymers, stretched in a rubbery state, may indeed undergo very large strains in a reversible way. This remarkable behaviour is often called rubber (or entropic) elasticity. The fundamental hypothesis of the molecular theory of rubber elasticity is that the variation of internal energy is proportional to the variation of the absolute temperature [14]. The analogy with ideal gases leads to an internal energy independent of the elongation, the stress being attributed to the so-called configuration entropy. As in classical elasticity, temperature T and strain ε are the chosen state variables. It was shown in Refs [14, 21] that for an entropic elasticity the free energy is of the form:

$$\psi(T,\varepsilon) = T\zeta(\varepsilon) + \eta(T) \qquad (3)$$

As shown in Ref. [16], the coupling sources derived from Equation (3) are equal to the deformation energy rate $w_{\text{def}}^{\bullet}$. These sources are negative when the specimen is unloaded and positive otherwise: this coupling term is in phase with the mechanical loading, contrary to the classical thermoelastic sources. This last property, the cyclic evolution of the overall heat source, and its very small asymmetry led the authors to claim the existence of a slightly dissipative competition between the two coupling effects. This kind of competition has already been observed in thermoplastic rubbers in the presence of a more noticeable intrinsic dissipation [16]. A natural continuation of this work would be the local analysis of the energy balance form within the neck shoulders using adapted optical lenses.

REFERENCES

1. Carothers, W. H. and Hill, J. W. (1932) Artificial fibers from synthetic linear condensation superpolymers. *J. Am. Chem. Soc.* **54**, 1579–1587.
2. Peterlin, A. and Olf, H. G. (1966) NMR observations of drawn polymers. Part. V. Sorption into drawn and undrawn polyethylene. *J. Polym. Sci. A* **4**, 587–598.
3. Gent, A. N. and Jeong, J. (1986) Plastic deformation of crystalline polymers. *Polym. Eng. Sci.* **26**, 285–289.
4. Strauch, V. and Schara, M. (1995) E.P.R. study of the orientation of polymer segments induced by cold drawing of a low density polyethylene. *Polymer* **36**, 3435–3438.
5. Waddon, A. J. and Karttunen, N. R. (2001) Structural transitions during the cold drawing of aliphatic ketone terpolymers. *Polymer* **42**, 2039–2044.
6. Honorat, V., Moreau, S., Muracciole, J.-M., Wattrisse, B. and Chrysochoos, A. (2005) Calorimetric analysis of polymer behaviour using a pixel calibration of an IRFPA camera. *Int. J. Quantitative Infrared Thermogr.* **2**, 153–172.
7. Chrysochoos, A., Wattrisse, B. and Muracciole, J.-M. (2000) Experimental analysis of strain and damage localization. In: *Symposium on Continuous Damage and Fracture* (A. Benallal, Ed.). Elsevier, Paris: 41–51.
8. Wattrisse, B., Muracciole, J.-M. and Chrysochoos, A. (2002) Thermomechanical effects accompanying the localised necking of semi-crystalline polymers. *Int. J. Therm. Sci.* **41**, 422–427.
9. Germain, P., Nguyen, Q.-S. and Suquet, P. (1983) Continuum thermodynamics. *J. Appl. Mech.* **50**, 1010–1020.
10. Thomson, W. (Lord Kelvin) (1857) On the thermo-elastic and thermo-magnetic properties of matter. *Quart. J. Math.* **1**, 00.
11. Joule, J. P. (1857) On some thermodynamic properties of solids. *Phil. Mag. (4)* **14**, 226.
12. Anthony, R. L., Caston, R. H. and Guth, E. (1942) Equations of state for naturals and synthetic rubber like materials: unaccelerated natural soft rubber. *J. Phys. Chem.* **46**, 826.

13. Wood, L. A. and Roth, L. R. (1944) Stress temperature relations in a pure gum vulcanizate of natural rubber. *J. Appl. Phys.* **15**, 781.
14. Chadwick, P. and Creasy, C. F. M. (1984) Modified entropic elasticity of rubberlike materials. *J. Mech. Phys. Sol.* **32**, 337–397.
15. Wattrisse, B., Chrysochoos, A., Muracciole, J.-M. and Nemoz-Gaillard, M. (2000) Analysis of strain localisation during tensile test by digital image correlation. *Expt. Mech.* **41**, 29–38.
16. Saurel, J.-L. (1999) Etude thermomécanique d'une famille d'élastomères thermoplastiques. PhD thesis, Montpellier University, France.
17. Chrysochoos, A. and Louche, H. (2000) An infrared image processing to analyse the calorific effects accompanying strain localisation. *Int. J. Eng. Sci.* **38**, 759–1788.
18. Ward, M. (1983) *Mechanical Properties of Solid Polymers*. John Wiley & Sons, London.
19. Batterman, S. D. and Bassani, J. L. (1990) Yielding anisotropy and deformation processing of polymers. *Polym. Eng. Sci.* **30**, 1281–1286.
20. G'Sell, C., Hiver, J. M., Dahoun, A. and Souahi, A. (1992) Video-controlled tensile testing of polymers and metals beyond the necking point. *J. Mat. Sci.* **27**, 5031–5039.
21. Ogden, R. W. (1992) On the thermoelastic modelling of rubberlike solids. *J. Therm. Stresses* **15**, 533–557.